An Oxide Wear Model of Ultrasonic Bonding

Brandon van Gogh[1], Tioga Benner[1], Henri Seppaenen[2], Calvin Tszeng[1], Panthea Sepehrband[1]

[1]Department of Mechanical Engineering, Santa Clara University,
Santa Clara, CA, 95053, USA
E-mail: bvangogh@scu.edu, bvangogh@alumni.scu.edu

[2]Kulicke & Soffa Industries, Inc.
Santa Ana, CA, 92705, US

Abstract
A modeling approach is developed to better describe the relation between input electrical power and the physical reaction of the bonding system during ultrasonic bonding. The major distinction between this analysis and previously published works is to attempt to eliminate empirically driven correlations between the input power and the kinetics of the bonding process. Two models, a piezoelectric model and an ultrasonic bonding model, are combined in order to reach this goal. The piezoelectric model is used to calculate the desired forcing, amplitude, and frequency that is created by the piezoelectric transducer during the actual ultrasonic bonding process. For this process, a lumped parameter model, taken from literature, is used, that converts input current and voltage to velocity and position of the bonding tooltip, respectively. This model is then combined with an updated model of the relative amplitude between the bonding material and substrate as the ultrasonic bond is being formed. Our model differs from existing friction power models by utilizing the Archard Equation to account for the removal of the natural oxide film. The integrated model provides a relationship between the bond growth and the driving power. The analysis enables comparison between the transverse force on the bond tool and amplitude of the bond tool's motion for different electrical input powers.

Key words
Ultrasonic Bonding, Wear, Oxide, Archard Equation

I. Introduction
Ultrasonic bonding is widely used in different industries, such as electronic packaging [1]. Obtaining a comprehensive model of ultrasonic bonding is an important step in uncovering a thorough understanding of the dependencies between process parameters and outcomes on both the microscopic and macroscopic scale. Several macroscopic models have been developed to describe different types of ultrasonic bonding. Finite Element Method (FEM) is commonly used to more closely model microscopic behaviors. Friction heating was modeled in ribbon bonding by assuming the friction power was caused by the shear stress at the interface [2]. An FEM model was used to determine the pressure distribution at the bonded interface. These FEM results were then used in a holistic model of the wedge-wedge wire bonding process [3]. Oxide fracture in wedge-wedge wire bonding was modeled using a shear lag model developed for cold rolling [4]

Another popular approach is to link the rate of bond growth to the friction power at the interface. A bond growth model by Mayer and Schwizer [5] was developed that can be used for determining the relative amplitude between the ball and substrate, and the ratio of unbonded interface area to the total interface area. It assumes that the rate of bond growth is proportional to the power supplied to the interface. It also lets the transverse force acting at the interface be composed of the friction and the shear strength of the bonds formed. These

two forces are weighted by the percentage of the unbonded and bonded areas respectively [5].

The model derived by Mayer-Schwizer [5] has been expanded upon. An equation was derived for the contact height [6] [7]. Experimental observations have been used to relate the ultrasonic transducer current to relative amplitudes in this model [8]. Recently, this model has been expanded to take into account the activated area to model ultrasonic cleaning [9].

In the present work, we propose to develop a modified version of the Mayer-Schwizer model that uses the Archard Equation to determine the relationship between the bond growth rate and wear. This model was conceived through earlier work about how the Archard wear Equation could be used to better understand oxide fracture [10]. Lumped parameters models also have been used to understand the system level dynamics of ultrasonic bonders [11]. A modified version of the lumped parameter piezoelectric model developed by Goldfarb and Celanovic [12] is used to model the ultrasonic transducer. The main purpose of this work is to present a modified modeling approach, which is less dependent on experimentally obtained parameters, and compare it to the existing model. The overall system level model is first reviewed. Then the procedure on how the Archard Equation is incorporated into the model is described.

II. Approach

The overall approach is to replace the relationship between the bond growth ratio and friction power used in the Mayer and Schwizer model with the Archard Equation. There are two sections of the model. The first section, referred to as the System Level model, accounts for the dynamics of the ultrasonic transducer. The second section, referred to as the Oxide Wear and Bond Growth model, replaces the friction power relationship in the Mayer and Schwizer model. This relationship is described briefly in this section.

A. System Level Model

The model of the entire bonding system is depicted in Figure 1 and Figure 2. The circuit depicted in Figure 1 is meant to capture the electrical side, while the diagram in Figure 2 is meant to capture the mechanical side

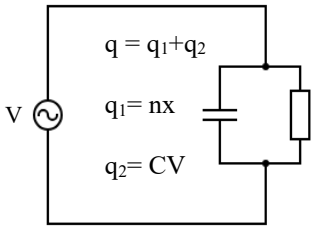

Figure 1*: Modified circuit based on Goldfarb Model [12].*

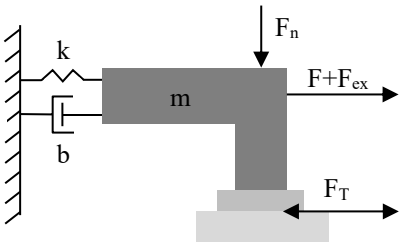

Figure 2: *Modified mechanical diagram based on Goldfarb Model to capture other components of bonding [5] [12].*

In Figure 2, F is the force produced by the transducer, m is the mass, b is the damping, k is the stiffness, C is the capacitance, n is the electromechanical transformation ratio, x is the position of the transducer and tool, F_n is the normal force, F_T is the transverse force, and V is the voltage supplied to the transducer. The charge across the piezoelectric transducer has two components, $q_1 = CV$ to account for the capacitive behavior of piezoelectric elements and $q_2 = nx$ to account for the mechanically induced charge. These diagrams give the following Equations:

$$m\ddot{x} + b\dot{x} + kx = F + F_T \quad (1)$$

$$F = nV \quad (2)$$

$$V = V_0 sin(\omega t) \quad (3)$$

$$I = n\dot{x} + C\dot{V} \quad (4)$$

where, ω is the angular frequency of the voltage signal, t is time, and I is the current. Despite the lumped piezo model only being valid below the first resonant frequency mode, it allows for an estimation of the current supplied to the transducer [12].

The transverse force given by the Mayer and Schwizer model is composed of the friction force μF_n and σ the shear strength of the bonds

$$F_T(t) = [1 - \gamma(t)]\mu F_n + \gamma(t)\sigma S \quad (5)$$

where $\gamma = \frac{S_{bonded}}{S}$ is the ratio of the bonded area S_{bonded} and the total interface area S [5]. γ acts as a way to weight the friction and shear strength of the bonds.

Another aspect of the Mayer-Schwizer model is the relationship between $A_{rel}(t)$, the free air vibration amplitude $A_0(t)$, the overall system compliance c, and $F_T(t)$ [5]

$$A_{rel}(t) = A_0(t) - cF_T(t) \quad (6)$$

The free air vibration amplitude is estimated using the free air response $x_0(t)$, or the solution to Equations (1)-(3) such that the transverse force is zero $F_T = 0$. The free air vibration with no initial displacement or velocity $x_0(0) = 0$, $\dot{x_0}(0) = 0$ is given by:

$$x_0(t) = C_0 cos(\omega t) + C_1 sin(\omega t) + [\, C_2 sin(\omega_d t) + C_3 cos(\omega_d t)] e^{-\zeta \omega_n} \quad (7)$$

$$C_0 = \frac{-b\omega_n V_o}{(k-\omega^2 m)^2+(b\omega)^2} \quad C_1 = \frac{(k-\omega^2 m) n V_0}{(k-\omega^2 m)^2+(b\omega)^2} \quad (8)$$

$$C_2 = \frac{-(C_1\omega+\zeta\omega_n C_0)}{\omega_d} \qquad C_3 = -C_0 \quad (9)$$

$$\omega_n = \sqrt{\frac{k}{m}} \quad \zeta = \frac{b}{2\sqrt{km}} \quad \omega_d = \omega_n\sqrt{1-\zeta^2} \quad (10)$$

where ω_n is the natural radial frequency, ω_d is the damped natural radial frequency, and ζ is the damping coefficient. With the free air vibration response, the free air vibration amplitude can be estimated using the steady state amplitude $A_{0,ss}$

$$A_{0,ss} = \sqrt{{C_0}^2 + {C_1}^2} \quad (11)$$

$$A_{0,est}(t) = \sqrt{{C_0}^2 + {C_1}^2}\ (1 - e^{-\zeta w_n}) \quad (12)$$

where $A_{0,est}(t)$ is an exponential estimation of how the free air vibration changes with time. Results with $A_0(t) = A_{0,ss}$ and $A_0(t) = A_{0,est}(t)$ are presented in the results section. The solution for the free air vibration can be found for different Voltage amplitudes V_0. The power applied to the transducer can be calculated as:

$$P = I_{rms} V_{rms} \quad (13)$$

where the root mean square is taken of both the current obtained from Equation (4) and the voltage from Equation (3).

B. Oxide Wear and Bond Growth

In the case of ultrasonic bonding, the surface oxide layer prevents bonding from occurring. In the Mayer-Schwizer model, these processes were accounted for using the following equation:

$$\dot{\gamma} = \frac{\beta}{S} P_{unbonded}(t) \quad (14)$$

where $P_{unbonded}(t)$ is the unbonded friction power and β is the bond growth coefficient [5] [6]. To use this equation, an experimentally determined value for β should be used.

To eliminate the dependency to experimental testing, the Archard Equation is used. The Archard Equation gives the oxide volume that is worn down due to the friction work that is supplied to the surface. This worn volume can be expressed in terms of the oxide wear height h and the total interface area S giving the following equation:

$$h = \frac{KF_n D}{HS} \quad (15)$$

where K is the wear is constant, D is the total sliding distance, and H is the material hardness [10]. A diagram of the bonding material-substrate contact is depicted in Figure 3. While the goal of this model is to look at ultrasonic bonding in general, the bonding material will be referred to as "ball" for convenience. As shown in the figure, $2L$ is the ball diameter, h_{oxide} is the initial oxide height, and x_b is the coordinate for describing the interface surface area.

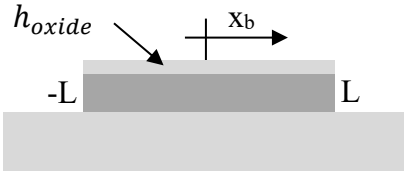

Figure 3: *Coordinates of Bonded Area.*

In developing the model, three assumptions are made, the first assumption, assumption (A1), is that the oxide wear height is a function of x_b and t or $h = h(x_b, t)$. Based on how the coordinate system is defined, the interface area is assumed to be rectangular such that $S = 2Lr$, where r is the width out of the page. To get the dependence upon x_b, we let the stress $F/S = W(x_b)/r$, where $W(x_b)$ is the force per

unit length. The ball diameter $2L$ is brought into the force to turn it into a force per unit length.

To get the dependence upon time it is assumed $D = D(t)$ such that

$$D(t) = \int_0^t 4fA_{rel}(t^*)[1-\gamma(t^*)]\,dt^* \qquad (16)$$

where $t^*$is a dummy integration variable. The unweighted velocity is $4fA_{rel}(t)$. The addition of the $4f$ is due to the fact that during one period, the ball moves 4 amplitudes in length. The weighting factor $[1-\gamma(t)]$ is to take into account that once the surface is completely bonded there is no more motion between the ball and the substrate [5].

The second major assumption, assumption (A2), is that once $h(x,t)$ reaches a critical value, i.e. h_{crit}, a bond forms. Assumption (2) is not far from what occurs in ultrasonic ball bonding. Surface oxides are removed due to the ultrasonic vibrations and the normal force. Before the ultrasonic vibrations begin, the normal force and the surface roughness of the ball and substrate lead to the formation of cracks in the oxide layer. After ultrasonic vibration, the cracks grow and the oxides eventually detach. These oxide particles move around the interface due to the ultrasonic vibration, tending to move out to the periphery [13]. Once this process occurs and the ball and substrate are separated by a small distance, i.e. h_{jump}, bonding occurs. Recently this jump to contact behavior for aluminum-aluminum bonding was simulated. It was found that the critical separation distance for jump to contact to occur is 5.8 Å ± 0.05 Å [14]. From this discussion, letting $|h_{jump}| = |h_{oxide} - h_{crit}|$ gives this the assumption of bond formation once $h(x_b,t) = h_{crit}$ some physical basis.

It is fair to point out that since $h_{oxide} > h_{crit}$, the model predicts that there will be an oxide layer with a thickness h_{jump} remaining, which in reality would prevent any bonding from occurring. This is because the Archard Equation does not account for the cracking and detachment of the oxide layer, or the motion of resulting oxide particles. Both of these processes lead to the exposed surfaces and jump to contact behavior. Since the oxides are not extracted from the interface during bonding, oxides particles are still present in the interface among micro-welds. The presence of oxide particles in bonded regions has been experimental confirmed [15]. To account for these processes would require a more thorough investigation that is beyond the scope of this work. Therefore, these processes are ignored when it is assumed that at $h(x_b,t) = h_{crit}$ bonding occurs.

Because $h(x_b,t)$ is a function of two variables, plotting all values $(x_b, t, h(x_b,t))$ in the domain of $-L \le x_b \le L$ and $0 \le t \le t_{max}$ will yield 3d surfaces. Constant values $h(x_b,t)$ result in level curves of these surfaces. These curves relate x_b and t together. When $h(x_b,t) = h_{crit}$, or when a bond forms, the exact position of where the bond forms will be given by x_b for a given time t. This leads to

$$h_{crit} = \frac{KW(x_{bonded})D(t)}{Hr} \qquad (17)$$

where x_{bonded} is the position of the growing bond area relative to x_b.

Because of the second assumption (A2), the form of $W(x_b)$ will determine how the bond grows. There have been several investigations on how the interface evolves in wedge-wedge wire bonding. Evidence suggests that bonding begins in the central regions for wedge-wedge wire bonding [15]. A second bonding pattern has also been reported that begins in the periphery and moves towards the center, greatly strengthening the bond [16]. In situ analysis of wedge-wedge bonding shows the total interface area S grows. The analysis also shows that there is both a static central region, where there is micro-weld bond growth among interspersed oxide particles, and a friction region that starts in the peripheral region. In the final stages of bonding, the strongest bonded areas are in the regions adjacent to the peripheral regions [17].

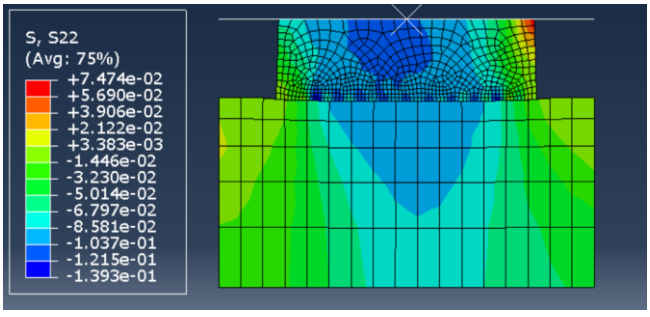

Figure 4: *FEM results for stresses at the interface in ball bonding for a load of 2.75 mN. The ball diameter is 34 µm and the stresses are in GPa [18].*

Based on these observations, the third major assumption, assumption (A3), assumes $W(x_b)$ is parabolic, with a local maximum at the center. Assumption (A3) is also supported by FEM analysis based on an unpublished work by Tszeng

[18]. The results are shown in Figure 4 and Figure 5. The stress achieves a maximum magnitude near the center. Also the stress near the ends of the ball, or at $L = 17\mu$m, is nearly zero.

Choosing a parabolic distribution also leads to bonding to start at the center and end in the peripheral regions, which is consistent with experimental results, assuming that the interface in ball bonding evolves similar to wedge-wedge. The parabolic distribution is

$$W(x_b) = A + B{x_b}^2. \tag{18}$$

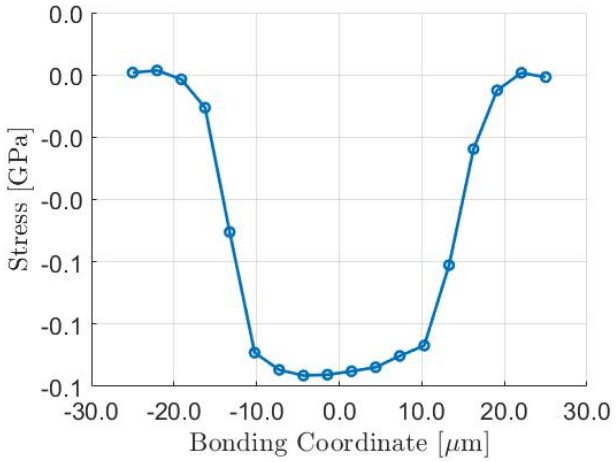

Figure 5: *Normal Stress distribution achieves a maximum value near the center of the bonding coordinate. The ball diameter is 34 μm.*

After making this third assumption (A3), Equations (17) and (18) can be used to solve for x_{bonded}:

$$x_{bonded} = \pm\sqrt{\frac{h_{crit}Hr}{KB}\frac{1}{D(t)} - \frac{A}{B}}. \tag{19}$$

From this it follows that the bonded area is $S_{bonded} = 2x_{bonded}r$. Therefore the bond growth ratio is given by

$$\gamma = \frac{x_{bonded}}{L}. \tag{20}$$

Using Equations (1)-(3) and (20), a complete state space model is found. After substituting Equation (19) into Equation (20) and using with $y_1 = x$, $y_2 = \dot{x}$, and $y_3 = \gamma$ the state space equations are

$$\dot{y_1} = y_2 \tag{21}$$

$$\dot{y_2} = -\frac{k}{m}y_1 - \frac{b}{m}y_2 + \frac{1}{m}F_T(t) + \frac{nV_0}{m}sin(wt) \tag{22}$$

$$\dot{y_3} = -\frac{2fK}{Hh_{crit}L^2rBy_3}(L^2B{y_3}^2 + A)^2A_{rel}(y_3)[1 - y_3]. \tag{23}$$

In order for the bond growth ratio to go to 1 as t goes to infinity it is necessary to enforce conditions on the bond growth ratio. Taking the limit of Equations (19) and (20) results in $\lim_{t\to\infty} x_{bonded} = \pm\sqrt{-\frac{A}{B}}$ and $\lim_{t\to\infty} y_3 = 1 = \frac{1}{L}\lim_{t\to\infty} x_{bonded}$. This gives the condition

$$B = -\frac{A}{L^2}. \tag{24}$$

If $W(0) = F_{max}/2L$ and $W(\pm L) = F_{min}/2L$, this gives

$$A = \frac{F_{max}}{2L} \tag{25}$$

$$B = \frac{F_{min} - F_{max}}{2L^3}. \tag{26}$$

Imposing these condition as t goes to infinity shows that F_{min} must be zero for $\gamma \to 1$ as $\to \infty$. This also matches the FEM results shown in Figure 5. F_{max} is then determined by integrating Equation (18) for $-L \le x_b \le L$. This gives $F_{max} = 3/2F_n$. Equations (21)-(23) are solved numerically for five voltages $V_0 = \{80,90,100,110,120\}V$ with $h_{crit} =$ 4.42nm and the following boundary conditions: $y_1(0) = 0$, $y_2(0) = 0$, and $y_3(0) = 0.05$. The initial bond growth ratio is set to a nonzero value to account for the cracks that form due to contact before ultrasonic vibration is applied [6]. This initial bond growth is equivalent to assuming there is an initial wear height h_{crit}. Also because of the presence of $1/y_3$in Equation (26), setting $y_3(0) = 0$ would result in an initially infinite bond growth rate. The constants used for the model are shown in Table **I**. These constants are presented for demonstration purposes. Most constants are taken from other work [12] [5] [10] [14] [6]. The spring constant k was set such that the transducer is resonating at $f = 130$ kHz by using Equation (10).

Table I: *Constants used for the model*

Variable	Value	Description
m	3.75 g*	Mass
b	150 Ns/m*	Damping
k	2.5 GN/m	Spring Stiffness
n	10*	Electro-Mechanical Ratio
C	1.2 µF*	Capacitance
c	1.33 µm/N **	Tool Compliance
S	207.5 mm^2 **	Interface Area
β	$55 \times 10^{-5} m^2/J$ **	Bond Growth Coefficient
F_n	0.15 **	Normal Force
µ	0.48 **	Coefficient of Friction
f	130,000 Hz**	Frequency
σ	125 Mpa **	Shear Strength of Bonds
h_{oxide}	5 nm ***	Initial Oxide Height
H	1400 kg/mm^2***	Oxide Hardness
K	1×10^{-5}***	Wear Constant
h_{jump}	5.8 Å ****	Jump to Contact Distance
$y_3(0)$	0.05 *****	Initial Bond Growth Ratio
V_o	{80,90,100,110,120} Volts	Input Voltage Amplitudes

* = from [12], **= from [5], ***= from [10], ****= from [14], *****=from [6]

III. Results and Discussion

The estimation of the free air vibration amplitude using $A_0(t) = A_{0,est}(t)$ in Equation (12), and the free air response using Equation (7) are both calculated with $V_0 = 100\,V$. As shown in Figure 6, $A_{0,est}(t)$ is a good estimation of the free air response amplitude. Using an exponential function in the form of $A_{0,est}(t)$ is similar to using a constant value, since the rise time is only about 10^{-4}seconds.

The relative amplitude as a function of the transverse force for the five voltage amplitudes are calculated using Equations (5) and (6). The relative amplitudes in Figure 7 are calculated using $A_0(t) = A_{0,est}(t)$ or Equation (12), while the relative amplitudes in Figure 8 use $A_0(t) = A_{0,ss}$ or Equation (11). For both Figures, the power is calculated using Equation (13).

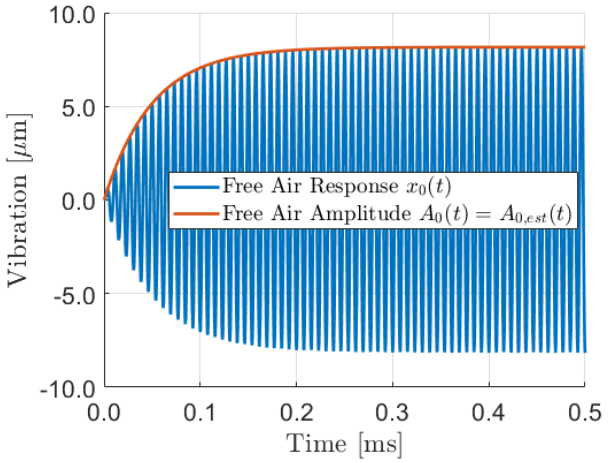

Figure 6: *The free air response and estimation of the free air amplitude for* $V_0 = 100\,V$.

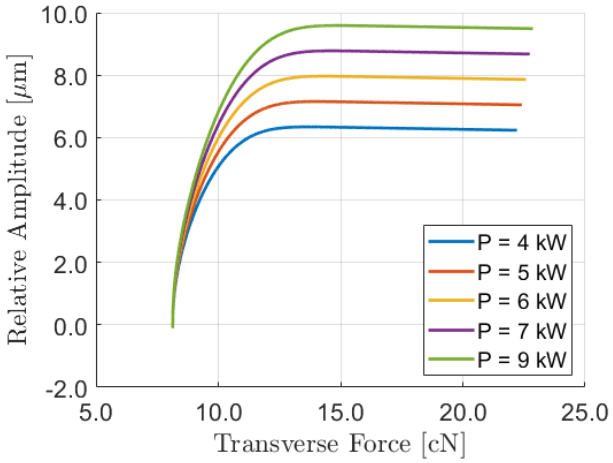

Figure 7: *Relative amplitude against the Transverse force for* $V_0 = \{80,90,100,110,120\}\,V$.

The results in Fig. 7 using $A_{0,est}(t)$ show the relative amplitude has two regions. In the first region the relative amplitudes sharply increase for nearly constant transverse forces. Initially the bond does not grow very fast, which causes the bonding ratio $\gamma(t)$ in Equation (5) to be nearly zero. At this stage the transverse force mostly comprises the friction force. In the second region, the relative amplitude is linear with respect to the transverse force. As the power increases, the relative amplitude increases since the transducer produces larger forces at higher powers. Also as the transverse force increases, the relative amplitude decreases since the transverse force restricts the motion of the ball.

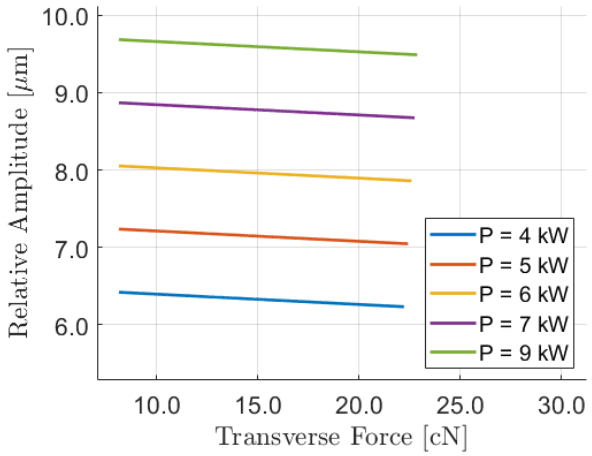

Figure 8: *The same plot as in Figure 7, when the free air vibration amplitude is set equal to the steady state amplitude ($A_0(t) = A_{0,ss}(t)$).*

There is only a linear region present in the results shown Fig. 8. This is because $A_{0,ss}$ is a constant, which does not account for when the transducer is initially starting up. Because $A_{0,ss}$ is also the steady state value of $A_{0,est}(t)$, results in the linear region in Figure 7 match the results in Figure 8.

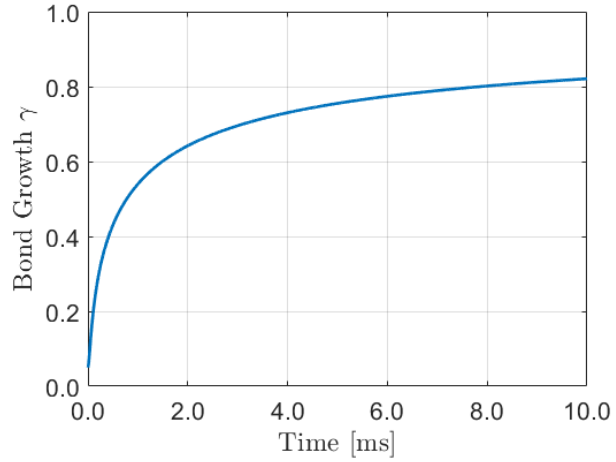

Figure 9: *The bond growth for the Archard Equation model for $V_0 = 100V$.*

The bond growth coefficient is calculated using Equations (21)-(23), or the Archard Equation model, and using the approach from the Mayer-Schwizer model. The results using the Archard Equation model are shown in Figure 9. The equivalent Equation (23) for the Mayer-Schwizer model is

$$\dot{y_3} = \frac{\beta 4 f \mu F_n}{S} A_{rel}(y_3)[1 - y_3]. \qquad (27)$$

Equation (27) follows from Equation (14). The results of the Mayer-Schwizer model are shown in Figure 10 using a $\beta = 55 \times 10^{-5}\text{m}^2/\text{J}$ [5]. Comparing Figure 9 and Figure 10, it can be seen that the bond growth for the Archard Equation model is much slower. It takes about 0.8 ms to achieve a γ of 0.5 for the Archard Equation model, while it takes about 0.04 ms to achieve a γ of 0.5 for the Mayer-Schwizer model.

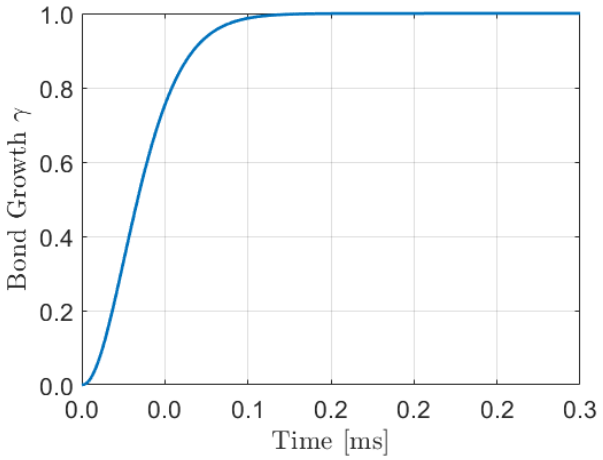

Figure 10: *The bond growth ratio for the Mayer-Schwizer model for $V_0 = 100\,V$ and $\beta = 55 \times 10^{-5}\,m^2/J$.*

This can be explained by determining the equivalent β, or β_{eq}, for the Archard Equation model. If it is assumed that Equation (27) and (23) are equal, the equivalent β for the Archard Equation model is

$$\beta_{eq} = -\frac{K}{Hh_{crit}LB\mu F_n y_3}(L^2 B {y_3}^2 + A)^2. \qquad (28)$$

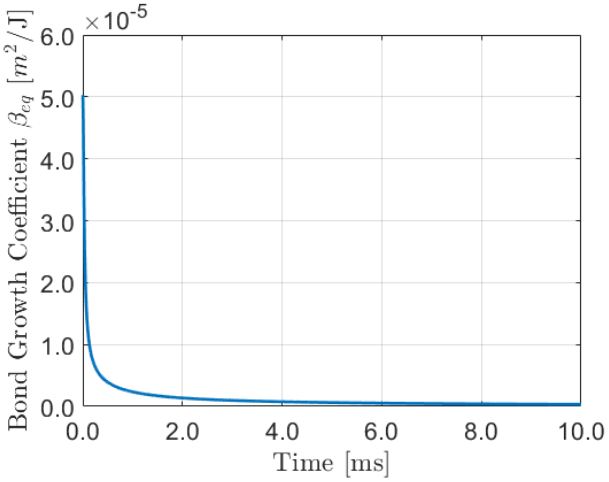

Figure 11: *β_{eq} for the Archard Equation model for $V_0 = 100\,V$.*

From Equation (28), Figure 11 is generated. Initially β_{eq} is calculated as $50 \times 10^{-6}\text{m}^2/\text{J}$. This value is one order of

magnitude smaller than the β used in the Mayer-Schwizer model, which explains why the bond growth is much slower for the Archard Equation model [5]. It is much slower also because β_{eq} is inversely proportional with time, as shown in Figure 11.

IV. Conclusions

In this work, a modeling approach was developed for ultrasonic bonding. The model uses lumped parameters to describe the kinetics of the transducer and tool, and the Archard Equation to describe oxide cleaning and bond growth. The modeling approach has three major assumptions: (A1) the oxide wear height a function of x_b and t $h(x_b, t)$, (A2) once $h(x_b, t) = h_{crit}$ oxide cleaning process is complete which allows a bond to form, and (A3) the normal force per unit length distribution is parabolic. Using an exponential estimation of the free air amplitude, the relative amplitude between the bonding material and the substrate was determined. It was found that as the power increases the relative amplitude increases, and that with larger transverse forces the relative amplitude decreases. Compared to the Mayer-Schwizer model, the Archard Equation model predicts a longer time for bond formation. The longer bond formation time is because the equivalent bonding coefficient is initially much smaller and is also inversely proportional to time. As a result, the bond increases at a slower rate compared to the Mayer-Schwizer model.

Several future adjustments can be made to the model; the constant parameters, such as the interface area S, could be replaced with functions, the model could be extended to a function of 3 variables with an additional bonding coordinate for the direction out of the page, equations could be introduced to account for stronger bonding in the periphery, and additional parameters, such as the initial surface roughness and contamination, could be brought into the model.

Acknowledgements

This work was supported by the National Science Foundation (CMMI-1728652).

References

[1] Y. Long, J. Tweifel and J. Wallaschek, "A review on the mechanisms of ultrasonic wedge-wedge bonding," *Journal of materials processing technology,* vol. 245, pp. 241-258, 2017.

[2] Y. Takahashi, M. Maeda, M. Ando and E. Yamaguchi, "Interfactial deformation and friction heating in ultrasonic Al ribbon bonding," *IOP Conference Series: Materials Science and Engineering,* vol. 61, 2014.

[3] T. Meyer, A. Unger, S. Althoff, W. Sextro, M. Brokelmann, M. Hunstig and K. Guth, "Modeling and Simulation of the Ultrasonic Wire Bonding Process," in *IEEE 17th Electronics Packaging and Technology Conference (EPTC)*, Singapore, 2015.

[4] B. Hsu, "Theoretical Investifation of Oxide Fracture during Ultrasonic Wedge Bonding.".

[5] M. Mayer and J. Schwizer, "Thermosonic Ball Bonding Model based on Ultrasonic Friction Power," in *IEEE Electronics Packaging Technology Conference*, 2003.

[6] H. Gaul, M. Schneider-Ramelow and H. Reichl, "Analytical Model Verification of the Interfactial Friction Power in AL us w/w Bondnig on Au Pads," *IEEE Transaction on Components and Packaging Technologies,* vol. 33, no. 3, 2010.

[7] H. Gaul, A. Shah, M. Mayer, N. Zhou, M. Schneider-Ramelow and H. Reichl, "The ultrasonic wedge/wedge bonding process investigated using in situ real-time amplitudes from laser vibrometer and integrated force sensor," *Microelectronic Engineering,* vol. 87, pp. 537-542, 2010.

[8] A. Shah, H. Gaul, M. Schneider-Ramelow, H. Reichl, M. Mayer and N. Zhou, "Ultrasonic Friction Power during Al Wire Wedge-Wedge Bonding."," *Journal of Applied Physics,* vol. 106, no. 1, pp. 13503-13511.

[9] R. Schemmel, C. Scheidemann, T. Hemsel, O. Kirsch and W. Sextro, "Experimental analysis and modelling of bond formation in ultrasonic heavy wire bonding," in *11th International Conference on Integrated Power Electronics Systems*, Berlin, Germany, 2020.

[10] H. Seppanen, A. Kaskela, K. Mustonen, M. Oinonen and E. Haeggstrom, "Understanding Ultrasonic-induced Aluminum Oxide Breakage During Wirebonding," in *IEEE Ultrasonics Symposium Proceedings*, New York, NY, 2007.

[11] A. Unger, W. Sextro, T. Meyer, P. Eichwald, S. Althoff and F. Eacock, "Modeling of the Stick-Slip Effect in Heavy Copper Wire Bonding to Determine and Reduce Tool Wear," in *2015 17th Electronics Packaging Technology Conference*.

[12] M. Goldfarb and N. Celanovic, "A Lumped Parameter Electromechanical Model for Describing the Nonlinear Behavior of Piezoelectric Actuators," *Journal of Dynamic Systems, Measurement and Control,* vol. 119, no. 3, 1997.

[13] Y. Long, F. Denecker, A. Isaak, J. Hermsdorf, M. Wurz and J. Twiefel, "Self-Cleaning Mechanisms in Ultrasonic Bonding of Al Wire," *Journal of Materials Processing Technology,* vol. 258, pp. 58-66, 2018.

[14] M. Khajehvand and P. Sepehrband, "The effect of crystallographic misorientation and interfacial separation on jump-to-conrtact behavior and defect generation in aluminum," *IOP Science.*

[15] M. Maeda, S. Kitamori and Y. Takahashi, "Interfacial Microstructure between THick Aluminum Wires and Aluminum Alloy Pads Formed by Ultrasonic Bonding," *Science & Technology of Welding & Joining,* vol. 18, no. 2, pp. 103-107, 2013.

[16] V. H. Winchell and H. M. Berg, "Enhancing Ultrasonic Bond Development," *IEEE Transaction on Components, Hybrids, and Manufacturing Technology,* vol. 1, no. 3, pp. 211-219, 1978.

[17] Y. Long, F. Denecker, A. Isaak, C. Li, M. Wurz, J. Twiefel and J. Wallashek, "Analysis of the Wire/Substrate Interface during Ultrasonic Bonding Process," in *IEEE CPMT Symposium Japan (ICSJ)*, Kyoto, Japan, 2017.

[18] C. Tszeng, "Analytical Solutions of Stresses in Fragmented Thin-Film on Contacting Surfaces: Applications to Ultrasonic Wire Bonding Process," 2020.